

Spin waves in a ferromagnetic topological metal

Wenliang Zhang¹, Teguh Citra Asmara¹, Yi Tseng¹, Junbo Li², Yimin Xiong^{3, 4}, Vladimir N. Strocov¹, Y. Soh^{5*}, Thorsten Schmitt^{1†}, and Gabriel Aeppli^{1, 6, 7}

¹*Photon Science Division, Paul Scherrer Institut, CH-5232 Villigen PSI, Switzerland*

²*Anhui Province Key Laboratory of Condensed Matter Physics at Extreme Conditions, High Magnetic Field Laboratory, Chinese Academy of Sciences, Hefei 230031, China*

³*Department of Physics, School of Physics and Optoelectronics Engineering, Anhui University, Hefei 230601, P. R. China*

⁴*Hefei National Laboratory, Hefei 230028, China*

⁵*Paul Scherrer Institut, CH-5232 Villigen PSI, Switzerland*

⁶*Laboratory for Solid State Physics and Quantum Center, ETH Zurich, CH-8093 Zurich, Switzerland.*

⁷*Institut de Physique, EPF Lausanne, CH-1015 Lausanne, Switzerland.*

To whom correspondence should be addressed: *yona.soh@psi.ch; †thorsten.schmitt@psi.ch

Abstract

In most metals, charges and spins can hop rapidly between atoms, yielding strong dispersion of their energy versus momentum. There are, however, special arrangements of atoms, such as twisted graphene bilayers or lattices which resemble woven bamboo “kagome” mats, so that particle motion with strong hopping between neighbours becomes nearly or even completely dispersionless, *i.e.*, the excitation energy is flat as a function of momentum. Such flat bands are interesting because the interactions between the heavy particles inhabiting them will become much more important than for strong dispersion, resulting in novel quantum solid and liquid states, particularly when topology enters on account of significant spin-orbit coupling for the underlying electrons. Nonetheless, spectroscopic evidence for flat bands engendered by lattice geometry rather than weak hopping is rare, particularly for metallic single crystals. Here we report the discovery, using circularly polarized X-Rays in resonant absorption and inelastic scattering (RIXS) for the unambiguous isolation of magnetic signals, of a flat spin wave band and large (compared to elemental iron) orbital moment for the metallic kagome ferromagnet Fe₃Sn₂, which has a topologically non-trivial electronic band structure controllable by modest external magnetic fields. The flat mode energy is consistent with the high Curie temperature ($T_C \approx 640$ K) as well as the strong acoustic mode dispersion, implying, together with the substantial spin-orbit coupling indicated by the large orbital moment, that the mode is topological. The measured properties of the spin waves are highly unconventional, and include very severe damping as well as the flat mode amplitude which is maximized in the long wavelength limit where it is ordinarily expected to vanish. Our results open the topic of interactions of topological bosons (spin waves) and fermions (electrons) with the very specific target of explaining boson lifetimes and amplitudes.

Introduction

Technology has long relied on transition metal-based ferromagnets, with their high Curie temperatures and many other convenient properties, such as tunable hardness, which allows a range of applications from motors to electrical transformer cores. The basic understanding of the magnetism of such compounds needed to await the development of the quantum theory of metals in the mid-twentieth century, and there continue to be surprises on the fundamental physics front. An example of an intermetallic compound consisting of two very common elements – iron and tin – which challenges even the contemporary quantum theory of solids is Fe_3Sn_2 .

Fe_3Sn_2 is a ferromagnet with a high Curie point $T_C \approx 640 \text{ K}$ ^{1–3} and consists of kagome bilayers stacked along c with the crystal structure belonging to the space group $R\bar{3}m(1)$ ⁴ (Fig. 1a). The kagome layers are composed of two different sets of equilateral triangles with different Fe-Fe distances as indicated by magenta and cyan bonds in Figure 1a⁴, and are stacked with an offset along the $(1, -1)$ in-plane lattice direction. The key questions concerning Fe_3Sn_2 follow from the first impression, based on the high temperature metallic ferromagnetism itself and the substantial Fe content, that the material is simply a diluted version of elemental iron. What speaks against this is that the kagome lattice arrangement is unusual, and so it is natural to ask first whether there is any physical property of the three-dimensional material, which approaches that of an ideal kagome system with short-range interactions. Of central importance here is the existence or not of clearly resolved flat bands for any charge or spin excitations. Magnetic moments grouped together within unit cells can precess to produce conventional ferromagnetic spin waves, whose energies grow with wavenumber on account of the increasing phase difference between neighbouring unit cells. There is also the possibility of optical spin waves, where magnetic moments within a unit cell rotate out of phase relative to each other. For the simple kagome lattice with only nearest neighbour interactions, such rotations can be made independently from those in neighbouring unit cells, meaning that they are local degrees of freedom giving rise to a flat spin wave band. Fig. 1b shows the calculated spin wave dispersion⁵ for the ideal kagome ferromagnet with its three Fe atoms per unit cell, bearing out one acoustic and two optic modes, one of them flat, and raising the first question concerning Fe_3Sn_2 , namely to what extent do the magnetic dynamics of this three-dimensional material approach those of the ideal kagome ferromagnet.

The second question concerns the orbital angular momentum \mathbf{L} in Fe_3Sn_2 that is almost entirely quenched for Fe. There has thus far been no direct measure of the orbital contribution to the magnetism, but there are numerous thermodynamic and electrical properties, which can only be understood if \mathbf{L} and the spin-orbit coupling are taken into account. Most prominent among these are a large anomalous Hall effect⁶ and a transition around 120 K where the preferred magnetization direction rotates from c towards the kagome planes on cooling. The latter has been a topic since 1970^{1,2,7}, with recent work unequivocally confirming that it is of first order and could be explained by the crossing of electronic free energies for the different magnetization directions^{8,9}. Theory including the spin-orbit interaction as a key ingredient predicts that new phases, such as states with fractionally charged quasiparticles, could emerge due to strong correlations in the flat bands^{10–12}. The most recent discoveries center on the very large number of topologically non-trivial band crossings of Weyl character, within 10 meV of the Fermi level¹³; for iron there are a handful of Weyl nodes but they are further away from the Fermi level¹⁴. Density functional calculations show that the disposition of Weyl nodes near the

Fermi level for Fe_3Sn_2 responds strongly to rotations of the magnetization, which accounts for observations that the electronic properties can be manipulated via application of modest external fields^{13,15,16}.

Notwithstanding many experimental and theoretical papers dealing with Fe_3Sn_2 , there are no clearly resolved spectroscopic data unambiguously confirming an impact of the kagome lattice geometry on either charge or spin degrees of freedom. In addition, the relative orbital and spin contributions to the magnetism are unknown. We have therefore used magnetic circular dichroism (MCD) of X-ray absorption spectroscopy (XAS) to establish the orbital component of the magnetic moment, and to perform resonant inelastic X-ray scattering (RIXS) to determine the magnetic Hamiltonian. The data reveal a much larger orbital contribution to the ferromagnetism than for elemental iron. Furthermore, employing MCD in RIXS measurements¹⁷, we identify both conventional acoustic spin waves, with stiffness similar to that found in the very low energy transfer (< 2 meV) limit by neutron scattering from powders¹⁸, as well as the dispersionless optic mode characteristic of kagome ferromagnets. As can be seen in Figure 1b, the wavenumber-dependent eigenfrequencies are entirely consistent with expectations for those of a single kagome plane with nearest neighbour exchange coupling accounting for both the acoustic mode stiffness and the flat optic mode. While the intensities of the acoustic mode agree with those for conventional insulating and metallic ferromagnets, those for the optic mode disagree dramatically, which again underlines the importance of spin-orbit effects in Fe_3Sn_2 .

To our knowledge, this is the first time that a flat optic spin-wave mode has been seen for a metallic kagome material and indeed for any single crystal ferromagnet of kagome type. Although the spin waves for a ferromagnetic kagome insulator have been measured for $\text{Cu}[1,3\text{-benzenedicarboxylate (bdc)}]$, a metal-organic compound hosting $S=1/2$ Cu^{2+} ions, using inelastic neutron scattering¹⁹, experiments were limited to powder specimens due to the unavailability of the large single crystals required for inelastic neutron scattering. Low frequency spin waves were observed by neutron scattering from single crystals of the metallic kagome ferromagnet $\text{Co}_3\text{Sn}_2\text{S}_2$ ^{20,21}, but the anticipated optical flat bands here are too high in energy to be reached by conventional cold or thermal neutron scattering. More recently, near-flat-band excitations were observed in $\text{Co}_3\text{Sn}_2\text{S}_2$ by RIXS²². However, instead of a spin-wave mode, the excitations are suggested to be Stoner excitations originating from electron-hole pairs between nearly flat electronic bands. RIXS does not suffer from the limitation on energy transfers, and by taking advantage of the circularly polarized photons produced at a modern synchrotron beamline, we can unambiguously identify the magnetic nature of the observed excitations.

Experiment and results

MCD-XAS and RIXS rely on the heightened sensitivity of X-ray absorption and scattering at elemental absorption lines due to transitions between atomic core levels and conduction bands near the Fermi level. Fig. 1c shows the experimental geometry for XAS and RIXS measurements. To observe MCD, a magnetic field (~ 0.13 T) along the $(H, 0)$ direction in the reciprocal space of the kagome planes is applied to align the magnetic domains in the sample. Figure 2 summarizes the XAS-MCD results on the Fe_3Sn_2 sample. The XAS data are collected by the total electron yield (TEY) method at different incident angles α and photon polarizations CL (left circular) and CR (right circular) at $T = 25$ K. Saturation effects are corrected to extract the absorption coefficient μ (see details in the Supplementary Material). XAS-MCD is maximized when the helicity vector for the photon is parallel to the sample magnetization. As

shown in Fig. 2a, μ shows no difference between CR and CL at normal incidence ($\alpha = 90^\circ$), while the difference increases with decreasing α from normal to grazing incidence. Figure 2b shows the normalized differences $[\mu(\alpha) - \mu(90^\circ)] / \cos \alpha$ as a function of α , showing a collapse onto two curves of equal magnitude and opposite sign determined by the sign of the photon helicity. Thus, the difference simply follows the factor $\cos \alpha$, consistent with the simplest theory for the variation of XAS-MCD with the angle between the helicity of the photon and sample magnetization \mathbf{M} . Using the $\cos \alpha$ factor, we can extrapolate the XAS-MCD to $\alpha = 0^\circ$ (helicity of photon fully parallel (CR) or anti-parallel (CL) to \mathbf{M}). Fig. 2c displays the result together with the previous XAS-MCD result for pure iron (thick blue lines)²³. Fe_3Sn_2 shows a larger dichroism at the L_3 -edge than pure iron. By the sum rules for XAS-MCD, the orbital and spin magnetic moments can be determined^{24,25}. We assess the orbital moment per hole of an iron site to be $m_{\text{orb}} \sim 0.1325 \mu_B$, and the spin moment per hole $m_{\text{spin}} \cdot (1 + \frac{7\langle T_z \rangle}{2\langle S_z \rangle}) \sim 0.6 \mu_B$, where $\langle T_z \rangle$ is the expectation value of the magnetic dipole operator and $\langle S_z \rangle$ is equal to half of m_{spin} in Hartree atomic units. While the spin moment m_{spin} in Fe_3Sn_2 is close to the value for pure iron, the orbital moment is much larger, with $m_{\text{orb}} / m_{\text{spin}} \sim 0.22$ in contrast to 0.043 for pure iron²³. This result reveals a large orbital component in the total magnetic moment of Fe_3Sn_2 .

Using a XAS-MCD sample scan at the absorption maximum, we characterized the moment alignment across the whole samples with (Fig. 2e) and without (Fig. 2f) an in-plane magnetic field. The measurement is done at $\alpha = 20^\circ$. As can be seen, the magnetic field of ~ 0.13 T polarizes the moments of the whole sample, which shows a large domain with homogeneous XAS-MCD signals, consistent with Fe_3Sn_2 being a soft ferromagnet with an easy axis along the kagome plane in the low temperature phase^{8,9}. On the other hand, the sample without magnetic field only shows weak XAS-MCD signals in small and discrete regions due to averaging of the MCD signal over oppositely magnetized domains owing to the large footprint ($\sim 100 \mu\text{m} \times 5 \mu\text{m}$) of the beam compared to the magnetic domain size⁹. The alignment of a large and homogeneous ferromagnetic domain with the magnetic field allows measurement of RIXS-MCD for a single magnetic domain. Fig. 2d shows a comparison of the RIXS spectra for samples with and without magnetic field. The former spectra show much more pronounced dichroism than the spectra taken without a field, with a peak around 0.15 eV being almost fully suppressed in CL incident polarization. We note that the peak close to zero energy also shows a pronounced dichroism. As non-Bragg elastic scattering has no MCD in a fully polarized crystalline ferromagnet, this peak must be derived from low-energy excitations with origin similar to that of the peak at 0.15 eV, which we identify as magnons in the analysis below.

Figure 3 presents the RIXS results for a single in-plane polarized magnetic domain of Fe_3Sn_2 at $T = 25$ K. The RIXS spectra are measured with the incident photon energy tuned close to the Fe L_3 -edge resonance ~ 707 eV. The displayed spectra are already corrected by the self-absorption factors with the outgoing absorption coefficients averaged among different polarizations (see the Supplementary Material). Fig. 3a shows the momentum-dependent spectra along the $(H, 0)$ direction in a full energy transfer range. Fig. 3b-d show the spectra for low-energy transfer along $(H, 0)$ and (H, H) directions, and with azimuthal (ϕ) rotation, respectively. The RIXS spectra can mainly be separated into two parts, a high-energy broad peak above 0.4 eV (centered around 2 eV) and low-energy peaks below 0.3 eV. To clarify the nature of these two response components, we measured an incident photon energy dependent RIXS map at an in-plane momentum $\mathbf{q}_{\parallel} = (0.123, 0)$, as shown in Fig. 3e. The high-energy peak shifts to higher energy transfer as the incident energy E_i increases, which is characteristic

for ‘fluorescence-like’²⁶ behaviour, while the low-energy peaks stay at fixed energy transfer. The latter Raman-like behaviour suggests a collective nature of the low-energy excitations²⁷. A clear RIXS-MCD effect, *i.e.*, different intensities for CL and CR helicity of the incident X-rays, appears for both the low- and high-energy excitations. However, the momentum or incident angle dependences of the MCD for the fluorescence and Raman-responses are markedly different. Fig. 3f displays the integrated MCD intensities in the low- (-0.1 – 0.3 eV) and high- (1.3 – 4 eV) energy ranges of spectra along (H , 0) direction (Fig. 3a), which are shown *vs.* the incident angle α . The high-energy dichroism follows a $\cos \alpha$ form similar to the XAS-MCD results, suggesting that this dichroism originates mainly from the absorption step in the RIXS process and is trivially proportional to the amount of core holes of the intermediate states created in the absorption step, while the final states are mostly irrelevant. In contrast, the low-energy dichroism depends only weakly on α , and still shows a large dichroism even close to normal incidence, where the dichroism in XAS disappears. This suggests that the excited final states of the low-energy excitations are also selectively chosen by the different photon helicities, and are responsible for the dichroism together with the intermediate states. When the magnetic field is rotated to lie perpendicular to the scattering plane, the entire MCD effect fades out gradually according to $\cos \phi$, as shown in fig. 3d.

The non-trivial RIXS MCD effect of the low-energy excitations encodes the specific nature of the final states in the change of orbital/spin momentum. The photon polarization dependence in RIXS cross-section allows us to resolve the nature of the excitations. In the approximation where core-hole excitations on different sites are uncorrelated, the RIXS cross-section can be written²⁸ as a sum of local terms representing the resonances responsible for MCD multiplied by photon polarization factors and correlation functions formed between magnetization operators at the magnetic atom sites. For spin wave scattering, to lowest order in the magnetization operators, this results in a (zero-temperature) cross-section proportional to

$$I \propto \sum_{\lambda'} |\langle \lambda' | \boldsymbol{\varepsilon}_0^* \times \boldsymbol{\varepsilon}_i \cdot \hat{\mathbf{M}}_{\mathbf{q}} | \lambda \rangle|^2 \cdot \delta(E_\lambda - E_{\lambda'} - \hbar\omega) \quad (1)$$

Here, $\boldsymbol{\varepsilon}_i$ and $\boldsymbol{\varepsilon}_0$ are polarization vectors for incident and outgoing photons, respectively. The operator $\hat{\mathbf{M}}_{\mathbf{q}}$ is the Fourier transform of the local magnetization operators $\hat{\mathbf{M}}(\mathbf{r})$, where $\mathbf{q} = \mathbf{k}_i - \mathbf{k}_0$ is the change of the photon momentum, $|\lambda\rangle$ is the ferromagnetic ground state, and $|\lambda'\rangle$ is an excited state, which can be a magnon. The validity of expression (1) for spin waves observed by RIXS has been extensively tested^{28–33}. For RIXS MCD in a Heisenberg ferromagnet, where we sum over outgoing polarizations while forming the difference between the two circular polarizations of the incident X-Rays, we use the notation of Fig. 1c for a single domain sample, and obtain (see the details in Methods section):

$$I_{\text{RIXS-MCD}} \propto \sin \beta \cdot \sin(\alpha + \beta) \cdot \cos \phi \cdot \text{Im}(S^{zy}(\mathbf{q}, \omega)) \quad (2)$$

where β is the angle between incident and outgoing photons, α and ϕ is the incident and azimuthal angle, respectively. $S^{zy}(\mathbf{q}, \omega)$ is the zy element of the dynamic spin-spin correlation function, which is imaginary. This is in contrast to neutron scattering, where the off-diagonal elements of $S(\mathbf{q}, \omega)$ cancel with each other due to the polarization factors for that technique³⁴. For energy loss spectra, *i.e.*, when photons lose energy in the sample to create excitations, $\text{Im}(S^{zy}(\mathbf{q}, \omega))$ is equal to $S^{yy}(\mathbf{q}, \omega)$ and $S^{zz}(\mathbf{q}, \omega)$. Equation (2) results in the simple angular dependence, $\sin(\alpha + \beta)$, for the RIXS MCD of spin wave excitations of a ferromagnet when,

as is common, β is fixed ($\beta = 50^\circ$ in our experiment). In Figure 3f, we show that the angle dependence of the low-energy excitations follows the $\sin(\alpha + 50^\circ)$ curve very well, which confirms the transverse (to the magnetization) spin-wave nature of these excitations.

Analysis of Spin Waves

Using the intensity differences between CR and CL polarizations, we can isolate the magnetic contributions to the RIXS cross-section for Fe_3Sn_2 by excluding the non-dichroic diffuse reflection, which gives rise to elastic peaks at zero energy loss. By correcting the intensity difference with the polarization factors of spin waves and the self-absorption effect (see details in the Supplementary Material), we thus obtain pure magnetic Raman signals, which we can compare to theories for the energies, damping, and intensities of spin waves in our sample. The most important result is that there is a peak with a momentum-independent maximum around 0.15 eV, which seems to broaden with increasing momentum. In addition, there is a low-energy acoustic mode, which moves away from zero energy as \mathbf{q} increases from 0 in the quadratic manner expected for ordinary spin waves. Given that we can only identify two peaks in the data, we fit to the convolution of the resolution function with the sum of two damped harmonic oscillators, each of form

$$S(\omega) = (n(\omega) + 1) \cdot \frac{\gamma\omega}{(\omega^2 - \omega_0^2)^2 + 4\gamma^2\omega^2} \quad (3)$$

The fitted peak positions are overlaid on Fig. 1b, which also displays the simulated spin wave dispersion by spinW package⁵ for a ferromagnetic Heisenberg model $\mathcal{H} = \sum_{\langle i,j \rangle} -J_1 \vec{S}_i \cdot \vec{S}_j$ with only a nearest-neighbour (NN) exchange interaction $J_1 = 24.7$ meV and $S = 1$ (detailed fitting results are presented in the figure S3 of the Supplementary Material). The excellent agreement between the simple single-parameter theory and the observed spin wave dispersion indicates that we can characterize each constant- \mathbf{q} spectrum by four numbers, namely the amplitudes and damping constants for the flat and acoustic modes, while the peak maximum positions can be fixed according to the Heisenberg model.

Fig. 4a shows the data fitted to this form, with $J_1 = 24.7$ meV optimized by minimizing the sum squared error for all the fitting spectra (for the complete fitting for all momenta, see figure S4 in the Supplementary Material). Fig. 4b and c display the integrated intensities and damping constants of the two modes, respectively. The results along $(-K, 2K)$ are from the (H, H) direction (Fig. 3c), which are equivalent by symmetry. One can see that the intensities are only weakly dependent on momentum, with a slight decrease at high momentum. Fig. 4d shows the simulated $\text{Im}(S^{zy}(\mathbf{q}, \omega) - S^{yz}(\mathbf{q}, \omega))$ by spinW package⁵ based on the linear spin wave theory broadened by a resolution function with a full-width-at-half-maximum (FWHM) of 74 meV. For acoustic spin waves in a ferromagnet, the matrix element is momentum-independent, while the optic modes are strongly momentum-dependent, vanishing as $q \rightarrow 0$ because in this limit they represent out-of-phase oscillations of the moments within each unit cell. This gives nearly zero spectral weight for the flat and dispersive optic modes in the first Brillouin zone as can be seen in Fig. 4d. However, this is totally at odds with what we find for Fe_3Sn_2 . As shown by the RIXS MCD intensity map in Fig. 4e and integrated intensities in Fig. 4b, the intensity of the optic modes is large at all wavelengths and actually has a broad peak as $q \rightarrow 0$. The remarkable deviation from a simple Heisenberg model implies that additional factors such as spin-orbit coupling and the itinerant nature of the system need to be considered to reconcile these results.

The kagome ferromagnet, with three Fe atoms per unit cell, should display, as shown in Fig. 1b and Fig. 4e, a second, dispersive optic mode in addition to the flat mode. If inversion symmetry is broken and there is spin-orbit coupling, Dzyaloshinskii-Moriya terms will be generated which make the acoustic and flat modes topologically non-trivial, while the dispersive optic mode is not so³⁵. As $q \rightarrow 0$, the two optic modes are degenerate, while at the highest momentum transfer in this experiment ($q = 0.46 \text{ \AA}$), the dispersive branch would be substantially (35 meV) below the flat mode. However, the combination of damping of both the flat and acoustic modes, together with instrumental broadening ($\sim 74 \text{ meV FWHM}$) will merge the dispersive optic and flat modes. While two (acoustic and flat optic) modes fit the data well, we also fit the constant-momentum spectra by the three modes with the peak positions fixed according to the dispersions from the Heisenberg model (the detailed comparison is presented in Figure S5 of the Supplementary Material). To further reduce the number of fitting parameters, the amplitudes and damping factors of the dispersive optic and flat mode are set to be the same. The obtained fits are acceptable for all data, but they provide a slightly worse description of the higher q data than the two-mode fitting in the sense that they replicate less well the rise of the optic mode spectrum above the tail of the heavily damped acoustic magnons. This is further borne out by fits, also at higher q , where we varied the intensities of the two optic modes separately, and discovered that the preferred intensity for the dispersive, non-topological optic mode is indistinguishable from zero, which it (as well as the intensity of the topological flat mode) would be (see Fig. 4d) if we were dealing with the simplest, insulating realization of a kagome ferromagnet.

The spin wave damping for the acoustic mode varies in proportion to q^4 for thermally excited spin waves in Heisenberg ferromagnets^{36,37}. The solid line in Fig. 4c displays the fitting of the damping of the acoustic mode by Pq^δ , where q is expressed in dimensionless reciprocal lattice units. The fitted result $\delta = 2.84 \pm 0.3$ is smaller than 4, while $P = 0.6 \pm 0.22 \text{ eV}$ is much larger than not only the small thermal energy $k_B T = 0.002 \text{ eV}$, but also the largest spin wave energy, namely that attained by the flat optic mode. The damping of the optic/flat mode follows a similar momentum dependence described by $P = 0.45 \pm 0.49 \text{ eV}$, $\delta = 2.75 \pm 0.96$ and a constant offset of $0.025 \pm 0.002 \text{ eV} \gg k_B T$. The magnitudes of P , seen for both optic and acoustic modes are therefore such that only electronic excitations outside the manifold of spin wave excitations that would be found for insulating model magnets could account for the damping.

Discussion

We have taken advantage of modern synchrotron-based X-ray technology to examine the magnetic order and excitations in the much-celebrated metallic kagome ferromagnet Fe_3Sn_2 , allowing direct comparison to both insulating kagome ferromagnets and metallic iron. The excitations follow spin wave dispersion relations for the simple kagome ferromagnet with a single exchange interaction J_1 between nearest neighbours in the kagome plane. In particular, $J_1 \cong 24.7 \text{ meV}$ accounts for both the stiffness of the acoustic spin waves and the frequency of the flat optic mode characteristic of the kagome lattice. Furthermore, the mean field Curie temperature, $T_{CMF} = \frac{zS(S+1)J}{3k_B}$, where $z = 4$ is the number of nearest neighbours, $S = 1$ is the spin number, and $k_B \cong 8.617 \times 10^{-5} \text{ eV/K}$ yields an estimated $T_{CMF} \approx 760 \text{ K}$. This, given the complexities of the real three-dimensional layered material, is in excellent agreement with the reported $T_C \approx 640 \text{ K}$.

While the model Hamiltonian describes magnon energies and T_C in a consistent way, it fails to explain other results which are very simple to state. First, the orbital contribution to the

magnetic moment is five times larger than in elemental iron where it is understood to be almost entirely quenched on account of the crystal field energies being larger than the spin-orbit interaction. This is of course a quantitative manifestation of the large spin-orbit coupling which also makes Fe_3Sn_2 a topological material, with numerous Weyl nodes¹³, and indeed suggests a method to calibrate the spin-orbit coupling strength SOC introduced “by hand” into DFT: SOC is simply varied to obtain the ratio of orbital to spin contributions to the magnetization.

Another outcome of our experiments is the exceptionally high spin wave damping when compared to “local moment” ferromagnets including classic insulators such as EuO ³⁸ but also the manganites³⁹. Iron and nickel display similarly high damping accountable in terms of spin-conserving (*i.e.*, without appeal to spin orbit effects) decay into electron-hole pairs^{40–43}, thus placing Fe_3Sn_2 firmly into the league of itinerant ferromagnets. The acoustic mode spectral weights are, to within experimental error, independent of momentum, a finding consistent with theory and experiment for both itinerant and local moment ferromagnets. On the other hand, the nearly momentum-independent spectral weight of the optic mode is entirely unexpected, and requires strong spin-orbit coupling for explanation: the excited states of the spins on the hexagons in the kagome lattice have zero structure factor as $q \rightarrow 0$ (analogous to the ground states of antiferromagnetic kagome compounds⁴⁴), and must be mixed with electron-hole pairs of finite total angular momentum to be visible in the long wavelength limit. That there is strong mixing of the optic modes with the electron-hole pair continuum is clear from their considerable damping even for $q \rightarrow 0$. A particularly interesting possibility is the coupling of spin excitations to ring currents^{45,46} in the planes of these topological materials. To our knowledge, calculations of resulting effects as well as considerations of what happens when topological electrons mix with topological bosons are unavailable, and we look forward to theoretical work which will pioneer their understanding.

Methods

Experiments

The XAS and RIXS experiments were carried out at the ADRESS beamline of the Swiss Light Source at the Paul Scherrer Institut^{47,48}. The overall instrument resolution of the RIXS measurements is ~ 74 meV full-width-at-half-maximum. Figure 1c displays the experimental set-up and the scattering geometry. The plate-shaped crystal was cleaved in ultra-high vacuum at $T = 25$ K to yield a clean and flat surface parallel to the a - b plane. The scattering plane (expanded by the incident (\mathbf{k}_i) and emitting (\mathbf{k}_o) photon wave vectors) is set perpendicular to the sample a - b plane, and intersects with the a - b plane at the $(H, 0)$ direction. The scattering angle is fixed at 130° . As the ferromagnetism has an easy axis in the a - b plane at low temperatures, a magnetic field ($\mathbf{B} \sim 0.13$ T) is applied by a pair of permanent magnets along the $(H, 0)$ direction to polarize the sample magnetic moments. Right (CR) and left (CL) circular polarized incident photons are employed for the measurements, while the polarizations of emitted photons in RIXS are not resolved. All the data were collected at base temperature ~ 25 K. The momentum transfer \mathbf{q} is denoted in reciprocal lattice units (r. l. u.), with lattice constants $a = b = 5.315$ Å and $c = 19.703$ Å.

Calculation of Polarization Factor

Let $\mathbf{P} = \boldsymbol{\varepsilon}_o^* \times \boldsymbol{\varepsilon}_i$, the equation (1) can be rewritten as:

$$I \propto \sum_{ab} P_a^* P_b \sum_{\lambda'} \langle \lambda | \hat{\mathbf{M}}_{\mathbf{q},a}^\dagger | \lambda' \rangle \langle \lambda' | \hat{\mathbf{M}}_{\mathbf{q},b} | \lambda \rangle \cdot \delta(E_\lambda - E_{\lambda'} - \hbar\omega) \quad (4)$$

where a and b stand for x, y, z , which are the indices of the vector elements. The formula is very similar to the magnetic scattering of neutrons³⁴, with only different polarization factors $P_a^* P_b$. As for neutron scattering, the second summation in the above formula is proportional to the spin-spin correlation function $S^{ab}(\mathbf{q}, \omega)$. In the linear approximation for a local moment ferromagnetic system, given that the spins are polarized in the x direction as in this experiment as shown by Figure 1c, only the diagonal elements S^{aa} , S^{yy} , and S^{zz} are non-zero. While S^{xx} contributes to the elastic scattering, S^{yy} , S^{zz} , S^{yz} and S^{zy} are related to the dynamic part, with $S^{yy} = S^{zz}$ and $S^{yz} = -S^{zy}$. In the scattering geometry as in Figure 1c, we can define the polarization vectors $\mathbf{\epsilon}_i$ and $\mathbf{\epsilon}_o$. For example, the CL and CR incident polarizations are $(-i \sin \alpha, 1, -i \cos \alpha)/\sqrt{2}$ and $(i \sin \alpha, 1, i \cos \alpha)/\sqrt{2}$, respectively. By summing over the possible outgoing polarizations $\mathbf{\epsilon}_o$, we finally obtain the cross-section proportional to:

$$I_{CL/CR} \propto [(\sin \alpha)^2 + (\sin(\alpha + \beta))^2] \cdot S^{zz}(\mathbf{q}, \omega) + (\sin \beta)^2 \cdot S^{yy}(\mathbf{q}, \omega) \\ (-/+)\sin \beta \cdot \sin(\alpha + \beta) \cdot iS^{yz}(\mathbf{q}, \omega)(+/-)\sin \beta \cdot \sin(\alpha + \beta) \cdot iS^{zy}(\mathbf{q}, \omega) \quad (5)$$

For energy loss spectra like RIXS, S^{zy} is imaginary and equal to iS^{yz} . If we further include the azimuthal rotation, a $\cos \phi$ factor is needed, which altogether results in the RIXS MCD formula as equation (2).

Data availability

The datasets generated during and/or analysed during the current study are available from the corresponding author on reasonable request.

References

1. Trumphy, G., Both, E., Djéga-Mariadassou, C. & Lecocq, P. Mössbauer-effect studies of iron-tin alloys. *Phys. Rev. B* **2**, 3477–3490 (1970).
2. Le Caer, G., Malaman, B. & Roques, B. Mössbauer effect study of Fe₃Sn₂. *J. Phys. F Met. Phys.* **8**, 323–336 (1978).
3. Fenner, L. A., Dee, A. A. & Wills, A. S. Non-collinearity and spin frustration in the itinerant kagome ferromagnet Fe₃Sn₂. *J. Phys. Condens. Matter* **21**, 452202 (2009).
4. Malaman, B., Roques, B., Courtois, A. & Protas, J. Structure cristalline du stannure de fer Fe₃Sn₂. *Acta Crystallogr. Sect. B* **32**, 1348–1351 (1976).
5. Toth, S. & Lake, B. Linear spin wave theory for single-Q incommensurate magnetic structures. *J. Phys. Condens. Matter* **27**, 166002 (2015).
6. Kida, T. *et al.* The giant anomalous Hall effect in the ferromagnet Fe₃Sn₂ - a frustrated kagome metal. *J. Phys. Condens. Matter* **23**, 112205 (2011).
7. Malaman, B., Fruchart, D. & Le Caer, G. Magnetic properties of Fe₃Sn₂. II. Neutron diffraction study (and Mössbauer effect). *J. Phys. F Met. Phys.* **8**, 2389–2399 (1978).
8. Kumar, N., Soh, Y., Wang, Y. & Xiong, Y. Magnetotransport as a diagnostic of spin reorientation: Kagome ferromagnet as a case study. *Phys. Rev. B* **100**, 214420 (2019).
9. Heritage, K. *et al.* Images of a First-Order Spin-Reorientation Phase Transition in a Metallic Kagome Ferromagnet. *Adv. Funct. Mater.* **30**, 1909163 (2020).
10. Tang, E., Mei, J. W. & Wen, X. G. High-temperature fractional quantum Hall states. *Phys. Rev. Lett.* **106**, 236802 (2011).

11. Sun, K., Gu, Z., Katsura, H. & Das Sarma, S. Nearly flatbands with nontrivial topology. *Phys. Rev. Lett.* **106**, 236803 (2011).
12. Neupert, T., Santos, L., Chamon, C. & Mudry, C. Fractional quantum Hall states at zero magnetic field. *Phys. Rev. Lett.* **106**, 236804 (2011).
13. Yao, M. *et al.* Switchable Weyl nodes in topological Kagome ferromagnet Fe_3Sn_2 . *arXiv*: 1810.01514 (2018).
14. Gosálbez-Martínez, D., Souza, I. & Vanderbilt, D. Chiral degeneracies and Fermi-surface Chern numbers in bcc Fe. *Phys. Rev. B* **92**, 085138 (2015).
15. Kumar, N., Soh, Y., Wang, Y., Li, J. & Xiong, Y. Tuning the electronic band structure in a kagome ferromagnetic metal via magnetization. *Phys. Rev. B* **106**, 045120 (2022).
16. Yin, J. *et al.* Giant and anisotropic many-body spin–orbit tunability in a strongly correlated kagome magnet. *Nature* **562**, 91–95 (2018).
17. Elnaggar, H. *et al.* Magnetic Contrast at Spin-Flip Excitations: An Advanced X-Ray Spectroscopy Tool to Study Magnetic-Ordering. *ACS Appl. Mater. Interfaces* **11**, 36213–36220 (2019).
18. Dally, R. L., Phelan, D., Bishop, N., Ghimire, N. J. & Lynn, J. W. Isotropic nature of the metallic kagome ferromagnet Fe_3Sn_2 at high temperatures. *Crystals* **11**, 307 (2021).
19. Chisnell, R. *et al.* Topological Magnon Bands in a Kagome Lattice Ferromagnet. *Phys. Rev. Lett.* **115**, 147201 (2015).
20. Liu, C. *et al.* Spin excitations and spin wave gap in the ferromagnetic Weyl semimetal $\text{Co}_3\text{Sn}_2\text{S}_2$. *Sci. China Physics, Mech. Astron.* **64**, 217062 (2021).
21. Zhang, Q. *et al.* Unusual Exchange Couplings and Intermediate Temperature Weyl State in $\text{Co}_3\text{Sn}_2\text{S}_2$. *Phys. Rev. Lett.* **127**, 117201 (2021).
22. Nag, A. *et al.* Correlation driven near-flat band Stoner excitations in a Kagome magnet. *Nat. Commun.* **13**, 7317 (2022).
23. Chen, C. T. *et al.* Experimental confirmation of the X-Ray magnetic circular dichroism sum rules for iron and cobalt. *Phys. Rev. Lett.* **75**, 152–155 (1995).
24. Thole, B. T., Carra, P., Sette, F. & Van Der Laan, G. X-Ray circular dichroism as a probe of orbital magnetization. *Phys. Rev. Lett.* **68**, 1943–1946 (1992).
25. Carra, P., Thole, B. T., Altarelli, M. & Wang, X. X-Ray circular dichroism and local magnetic fields. *Phys. Rev. Lett.* **70**, 694–697 (1993).
26. Bisogni, V. *et al.* Ground-state oxygen holes and the metal-insulator transition in the negative charge-transfer rare-earth nickelates. *Nat. Commun.* **7**, 13017 (2016).
27. Minola, M. *et al.* Collective nature of spin excitations in superconducting cuprates probed by resonant inelastic X-Ray scattering. *Phys. Rev. Lett.* **114**, 217003 (2015).
28. Haverkort, M. W. Theory of resonant inelastic X-Ray scattering by collective magnetic excitations. *Phys. Rev. Lett.* **105**, 167404 (2010).
29. Ament, L. J. P., Van Veenendaal, M., Devereaux, T. P., Hill, J. P. & Van Den Brink, J. Resonant inelastic X-Ray scattering studies of elementary excitations. *Rev. Mod. Phys.* **83**, 705–767 (2011).

30. Braicovich, L. *et al.* Magnetic excitations and phase separation in the underdoped $\text{La}_{2-x}\text{Sr}_x\text{CuO}_4$ superconductor measured by resonant inelastic X-Ray scattering. *Phys. Rev. Lett.* **104**, 077002 (2010).
31. Guarise, M. *et al.* Measurement of magnetic excitations in the two-dimensional antiferromagnetic $\text{Sr}_2\text{CuO}_2\text{Cl}_2$ insulator using resonant X-Ray scattering: Evidence for extended interactions. *Phys. Rev. Lett.* **105**, 157006 (2010).
32. Schlappa, J. *et al.* Spin-orbital separation in the quasi-one-dimensional Mott insulator Sr_2CuO_3 . *Nature* **485**, 82–85 (2012).
33. Dean, M. P. M. *et al.* Spin excitations in a single La_2CuO_4 layer. *Nat. Mater.* **11**, 850–854 (2012).
34. Squires, G. L. *Introduction to the theory of thermal neutron scattering*. (Cambridge University Press, 2012). doi:10.1017/CBO9781139107808.
35. Zhang, L., Ren, J., Wang, J. S. & Li, B. Topological magnon insulator in insulating ferromagnet. *Phys. Rev. B* **87**, 144101 (2013).
36. Dyson, F. J. General Theory of Spin-Wave Interactions. *Phys. Rev.* **102**, 1217–1230 (1956).
37. Dyson, F. J. Thermodynamic Behavior of an Ideal Ferromagnet. *Phys. Rev.* **102**, 1230–1244 (1956).
38. Mook, H. A. Temperature Dependence of the Spin Dynamics of EuO. *Phys. Rev. Lett.* **46**, 508–511 (1981).
39. Perring, T. G. *et al.* Spin waves throughout the Brillouin zone of a double-exchange ferromagnet. *Phys. Rev. Lett.* **77**, 711–714 (1996).
40. Brookes, N. B. *et al.* Spin waves in metallic iron and nickel measured by soft X-Ray resonant inelastic scattering. *Phys. Rev. B* **102**, 064412 (2020).
41. Cooke, J. F., Lynn, J. W. & Davis, H. L. Calculations of the dynamic susceptibility of nickel and iron. *Phys. Rev. B* **21**, 4118–4131 (1980).
42. Mook, H. A. & Nicklow, R. M. Neutron scattering investigation of the magnetic excitations in iron. *Phys. Rev. B* **7**, 336–342 (1973).
43. Pelliciari, J. *et al.* Tuning spin excitations in magnetic films by confinement. *Nat. Mater.* **20**, 188–193 (2021).
44. Lee, S. H. *et al.* Spin-glass and non-spin-glass features of a geometrically frustrated magnet. *Europhys. Lett.* **35**, 127–132 (1996).
45. Varma, C. Non-Fermi-liquid states and pairing instability of a general model of copper oxide metals. *Phys. Rev. B* **55**, 14554–14580 (1997).
46. Bulaevskii, L. N., Batista, C. D., Mostovoy, M. V. & Khomskii, D. I. Electronic orbital currents and polarization in Mott insulators. *Phys. Rev. B* **78**, 024402 (2008).
47. Ghiringhelli, G. *et al.* SAXES, a high resolution spectrometer for resonant x-ray emission in the 400-1600 eV energy range. *Rev. Sci. Instrum.* **77**, 113108 (2006).
48. Strocov, V. N. *et al.* High-resolution soft X-ray beamline ADDRESS at the Swiss Light Source for resonant inelastic X-ray scattering and angle-resolved photoelectron

spectroscopies. *J. Synchrotron Radiat.* **17**, 631–643 (2010).

Acknowledgements: The experiments were performed at the ADRESS beamline of the Swiss Light Source at the Paul Scherrer Institut (PSI). The experimental work at PSI is supported by the Swiss National Science Foundation through project no. 200021 178867, and the Sinergia Network Mott Physics Beyond the Heisenberg Model (MPBH) (SNSF Research Grants CRSII2 160765/1 and CRSII2 141962). T.C.A. acknowledges funding from the European Union’s Horizon 2020 research and innovation programme under the Marie Skłodowska-Curie grant agreement No.701647 (PSI-FELLOW-II-3i program). G.A. was supported by the European Research Council under the European Union’s Horizon 2020 research and innovation programme HERO (Grant agreement No. 810451). Y.X. acknowledges funding from the Innovation Program for Quantum Science and Technology (No. 2021ZD0302802).

Competing interests: The authors declare no competing interests.

Author contributions: G.A. conceived the project. J.L. grew and characterized the single crystals with support from Y.X. W.Z., T.C.A., Y.T., and T.S. performed the RIXS experiments with the support of V.S. W.Z. analysed the data in discussion with Y.S., T.S., and G.A. W.Z., Y.S., T.S., and G.A. wrote the manuscript. Y.S., T.S., and G.A. coordinated the research.

Additional Information: Supplementary Information is available for this paper.

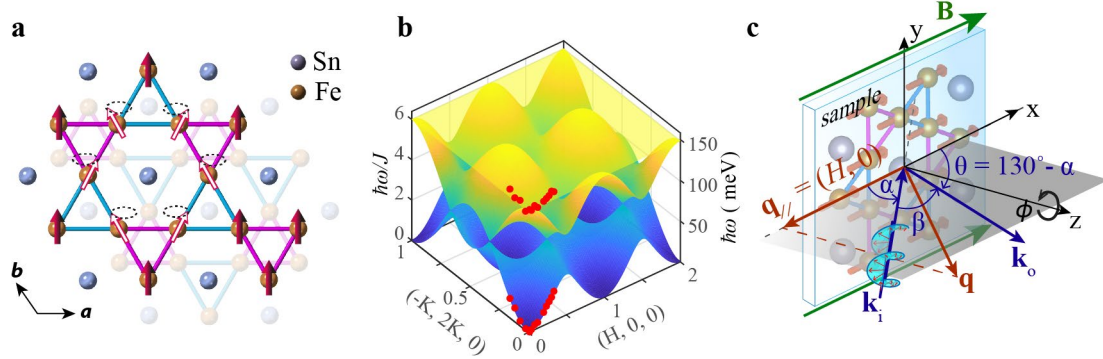


Fig. 1 Structure, spin wave dispersions, and experimental geometry for Fe_3Sn_2 . **a**, The kagome bilayer structure of Fe_3Sn_2 . The red arrows indicate the spins of iron; the white arrows on the hexagon represent a spin excitation whose localization accounts for the flat dispersion. **b**, Spin wave dispersion in $(H, 0) \times (-K, 2K, 0)$ plane, simulated by a Heisenberg model with nearest-neighbour (NN) interaction $J_1 = 24.7$ meV; the red dots are the peak frequencies for the experimental spectra (Fig. 4a) from a two-peak fitting. **c**, Scattering geometry and sample orientation in the experiment. The plate-shaped sample (cyan block) stands perpendicular to the scattering plane (gray plane). α and θ are the incident and emission angle of the X-rays, respectively. \mathbf{q} is the total momentum transfer and \mathbf{q}_{\parallel} is the projection of \mathbf{q} in the sample a - b plane. x , y , z are directions of sample translation in sample scans displayed in Fig. 2e and f. An in-plane magnetic field \mathbf{B} is applied to the sample as displayed by the green arrows and the red arrows on Fe atoms indicate the direction of the magnetic moments.

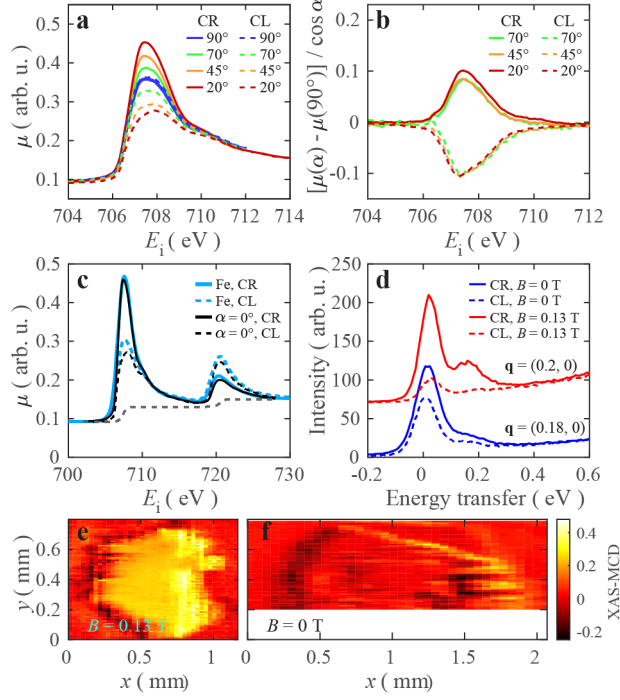


Fig. 2 Magnetic circular dichroism of X-ray absorption spectra. **a**, Absorption coefficients μ of Fe_3Sn_2 under an in-plane magnetic field (~ 0.13 T) at different incident angles (α) and circular polarizations (CR and CL), extracted from X-ray absorption spectra measured by total electron yield (TEY) method (see Supplementary Material). **b**, The difference between μ at a certain angle α and μ at $\alpha = 90^\circ$, scaled by a factor of $\cos \alpha$. **c**, The extrapolated absorption coefficients μ ($\alpha = 0^\circ$) of Fe_3Sn_2 (black lines) for CR and CL polarization. The thick blue lines are the absorption coefficients of pure iron²³. The gray dashed line is a simple two-step-like function for removing L_3 and L_2 edge jumps. The height of the step at L_3 is twice of the height at L_2 edge²³. **d**, RIXS spectra measured on a sample with in-plane magnetic field (red curves, $\alpha = 40^\circ$) and without magnetic field (blue curves, $\alpha = 43^\circ$). **e** and **f** show the XAS-MCD signals ($(\text{TEY}_{\text{CR}} - \text{TEY}_{\text{CL}}) / (\text{TEY}_{\text{CR}} + \text{TEY}_{\text{CL}})$) at Fe L_3 -edge resonance scanned across the sample surface with and without magnetic field, respectively. The incident angle α is 20° . The scan step along x is 0.03 mm and 0.06 mm for (e) and (f), respectively, and 0.01 mm along y for both. The x and y directions are depicted in Fig. 1c.

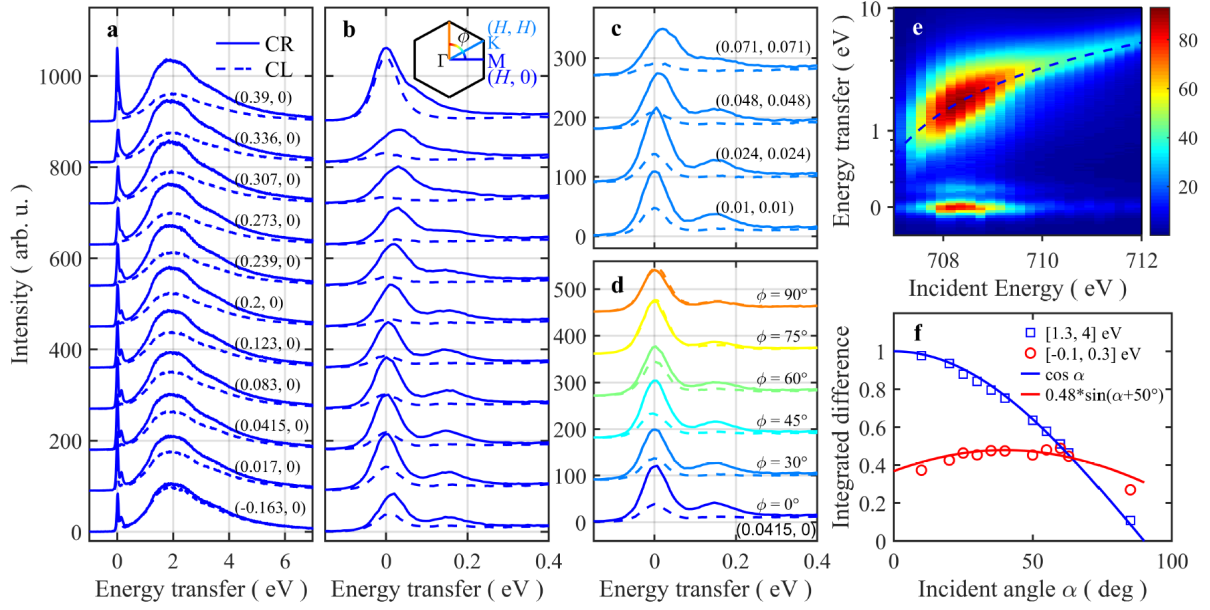


Fig. 3 RIXS spectra with momentum and incident energy dependence. **a-d**, RIXS spectra with CR and CL polarizations at Fe L_3 resonance: **a** and **b** along $(H, 0)$ direction, **c** along (H, H) , and **d** at different azimuthal angles. The inset hexagon in **b** indicates the Brillouin zone and the lines indicate the momentum directions. **e**, The RIXS intensity map as a function of energy transfer and incident energy for CR polarization; the y-axis is in a logarithmic scale, and the dashed line indicates a linear dependence on the incident energy. **f**, Integrated intensities of RIXS MCD in **a**, in an energy interval $[1.3 \text{ eV}, 4 \text{ eV}]$ (blue squares) and $[-0.1 \text{ eV}, 0.3 \text{ eV}]$ (red circles) as a function of incident angle α . The blue line is a curve of $\cos \alpha$, and the red line is $0.48 \cdot \sin(\alpha + 50^\circ)$. The integrated intensities are divided by the size of the integrated energy interval, and normalized by a scaling factor so that the fitting prefactor of the blue squares to $\cos \alpha$ is 1.

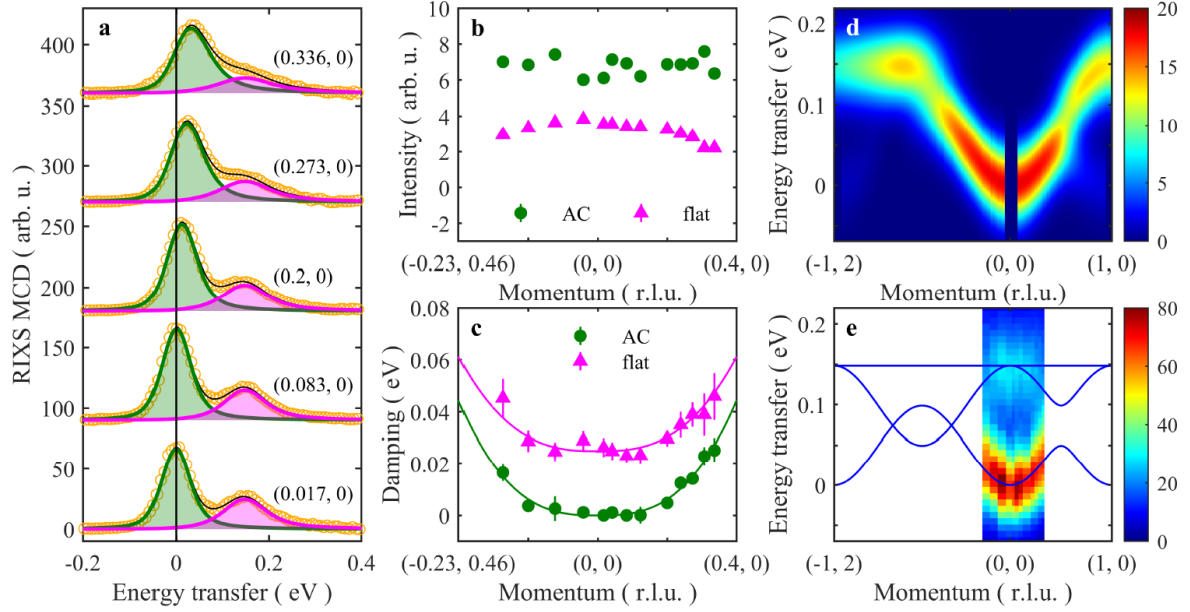


Fig. 4 Spin-wave fittings on the RIXS magnetic circular dichroism. **a**, RIXS intensity differences between CR and CL polarizations (RIXS MCD) at low-energy range (orange circles). The results are already corrected by polarization and self-absorption factors as described in the Supplementary Material. The black curves are the fits by two damped harmonic oscillators convolved with a resolution function (see Supplementary Material), and the green and magenta curves indicate the fitted acoustic and flat modes, respectively. The dispersion is fixed according to the Heisenberg model with a single nearest neighbour coupling in the fitting. The complete momentum dependent RIXS MCD and fitting are presented in Supplementary Figure S4. **b**, The integrated intensities of the fitted spin-wave modes; the green circles and magenta triangles indicate the acoustic (AC) mode and flat mode, respectively. **c**, Momentum dependence of the fitted damping factors of the acoustic and flat modes. The green solid line corresponds to Pq^δ with $\delta = 2.84$, and \mathbf{q} in reciprocal lattice units defined such that (1, 0) occurs at 1.365 \AA^{-1} . The magenta solid line represents the same form but with a constant offset. The error bars indicate the fitting errors of the parameters. **d**, Spin-spin correlations $Im(S^{zy}(\mathbf{q}, \omega) - S^{yz}(\mathbf{q}, \omega))$ simulated on a Heisenberg model with nearest-neighbour (NN) interaction $J_1 = 24.7 \text{ meV}$ based on the linear spin wave theory. **e** Intensity map of RIXS MCD as a function of momentum; the blue curves are the simulated spin wave dispersions in the Heisenberg model.

Supplementary material for Spin waves in a ferromagnetic topological metal

Wenliang Zhang¹, Teguh Citra Asmara¹, Yi Tseng¹, Junbo Li², Yimin Xiong^{3, 4}, Vladimir N. Strocov¹, Y. Soh^{5*}, Thorsten Schmitt^{1†}, and Gabriel Aeppli^{1, 6, 7}

¹*Photon Science Division, Paul Scherrer Institut, CH-5232 Villigen PSI, Switzerland*

²*Anhui Province Key Laboratory of Condensed Matter Physics at Extreme Conditions, High Magnetic Field Laboratory, Chinese Academy of Sciences, Hefei 230031, China*

³*Department of Physics, School of Physics and Optoelectronics Engineering, Anhui University, Hefei 230601, P. R. China*

⁴*Hefei National Laboratory, Hefei 230028, China*

⁵*Paul Scherrer Institut, CH-5232 Villigen PSI, Switzerland*

⁶*Laboratory for Solid State Physics and Quantum Center, ETH Zurich, CH-8093 Zurich, Switzerland.*

⁷*Institut de Physique, EPF Lausanne, CH-1015 Lausanne, Switzerland.*

To whom correspondence should be addressed: *yona.soh@psi.ch; †thorsten.schmitt@psi.ch

I. X-ray absorption

The X-ray absorption spectra (XAS) are measured in the total electron yield (TEY) mode by recording the drain current from the sample. The relation between TEY and the absorption coefficient μ in a bulk sample can be described by¹⁻³:

$$\text{TEY}(E_i, \alpha) = M \frac{\mu(E_i, \epsilon) l_e}{\sin \alpha} \cdot \frac{1}{1 + \mu(E_i, \epsilon) l_e / \sin \alpha} \quad (\text{A1})$$

where M is a constant depending on the material and the intensity of the incident photons, E_i is the incident photon energy, ϵ is the photon polarization, l_e is the electron escape depth, and α is the incident angle. When $\mu l_e / \sin \alpha \ll 1$ (l_e is much smaller than the photon penetration depth $l_p = \sin \alpha / \mu$), TEY is simply proportional to μ . This is usually true in transition metals around the L edge with not too small α . However, this condition is not fully met when E_i is close to the absorption edge (where μ becomes large) and α is small (grazing incidence), which will reduce the signal of TEY and thus distort the proportionality between TEY and μ as E_i is varied, known as the saturation effect. The exact μ is determined by the measured TEY as:

$$\frac{\mu(E_i, \epsilon) l_e}{\sin \alpha} = \frac{\text{TEY}(E_i, \alpha) / M}{1 - \text{TEY}(E_i, \alpha) / M} \quad (\text{A2})$$

We first measured the XAS with linear vertical (σ) polarization at several different α 's to estimate M , see Figure S1a. Figure S1b shows the angle dependence of the TEY $\cdot \sin \alpha$ at the pre-edge (blue circles, $E_i = [704, 705]$ eV) and resonance (red squares, $E_i = [707.3, 707.9]$ eV), and the solid lines are fitted by $M \cdot r / (1 + r / \sin \alpha)$ (see equation A1), where $r = \mu l_e$, and M are both varied. Figure S1c shows the fitted M at different E_i . Here, we take the weighted average as the value of M , where the weights are the amplitudes of TEY at normal incidence. Figure S1d shows the measured XAS around Fe L_3 edge for circular polarizations at different angles. Using equation A2 and the value of M , we then obtain new estimates for μl_e . The

results are plotted in figure S1e, with the error bars representing the change of the curve shape caused by the deviation from the average M value by a standard error.

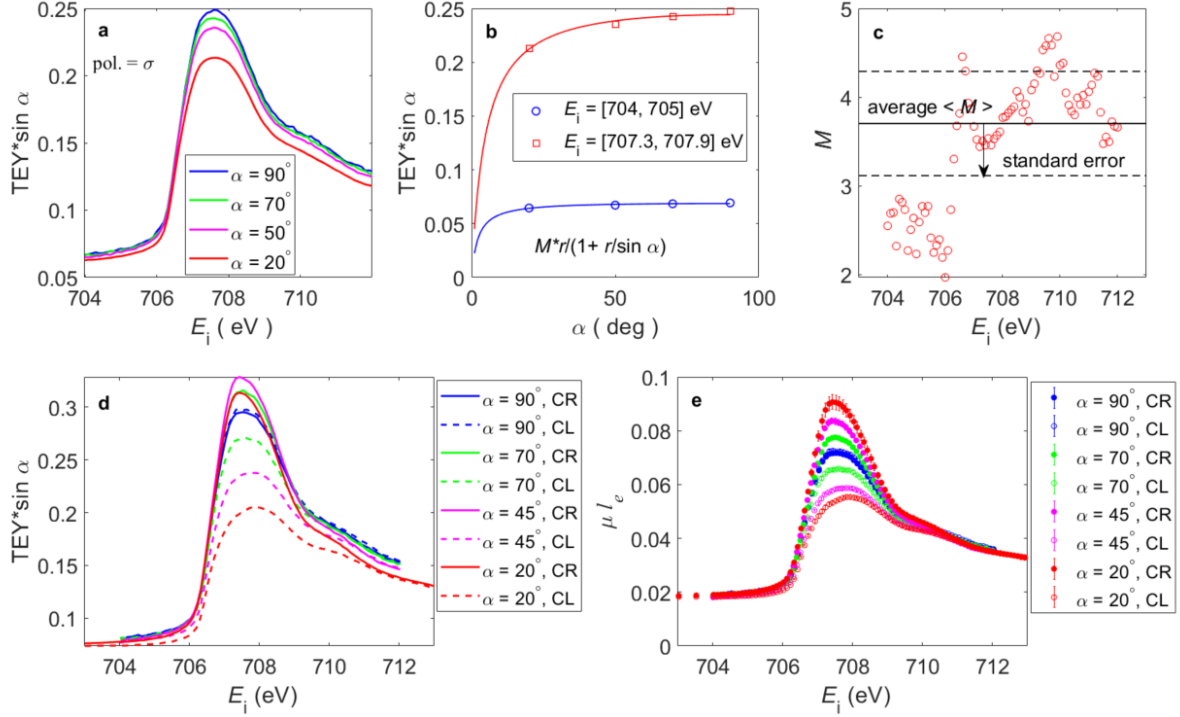


Figure S1. (a) XAS measured by TEY with σ polarization at different incident angle α . (b) Incident angle dependence of $\text{TEY} \cdot \sin \alpha$ at pre-edge energy (averaged in $E_i = [704, 705]$ eV, blue circle) and at resonance energy (averaged in $E_i = [707.3, 707.9]$ eV, red square); the solid lines are fitted by $M \cdot r / (1 + r / \sin \alpha)$. (c) The fitted M values as a function of incident energy; the solid black line indicates the weighted average value, and the dashed lines indicate a standard error deviation. (d) The measured XAS with circular polarizations at different incident angles. (e) The corrected μl_e according to equation A2.

II. Self-absorption correction of the RIXS spectra on the whole energy range

The self-absorption effect in RIXS spectra is corrected according to^{4,5}:

$$I_{\text{exp}}(E, \epsilon_i) = \sum_{\epsilon_o} \frac{I_c(E, \epsilon_i, \epsilon_o)}{\mu(E_i, \epsilon_i, \mathbf{k}_i) + \mu(E_o, \epsilon_o, \mathbf{k}_o) \cdot \sin \alpha / \sin \theta} \quad (\text{A3})$$

Here, α and θ are the incident and outgoing angles, respectively (Figure 1c), $E = E_i - E_o$ is the energy transfer, and I_c is the intrinsic RIXS cross section without self-absorption. Since the outgoing polarization (ϵ_o) is not resolved, the experimental result (I_{exp}) sums all ϵ_o . The absorption coefficient and its angle dependence are determined by the XAS as described in section I. above. Figure S2 shows the angle dependence of the denominator in equation A3 for CL and CR outgoing polarization and their ratio at $E = 0.1$ eV. The difference between the two outgoing polarizations is relatively small in the studied momentum range. For even higher energy, the difference in μ with different polarizations become even smaller. It is therefore a good approximation to use the average $\mu(E_o, \epsilon_o, \mathbf{k}_o)$ of the two outgoing polarizations in the denominator. The summation symbol then only applies to the numerator, and we can get the intrinsic RIXS cross-section $\sum_{\epsilon_o} I_c(E, \epsilon_i, \epsilon_o)$ by simply multiplying the experimental RIXS

spectra I_{exp} with the denominator. The spectra corrected in this way are shown in Fig. 3 in the main text.

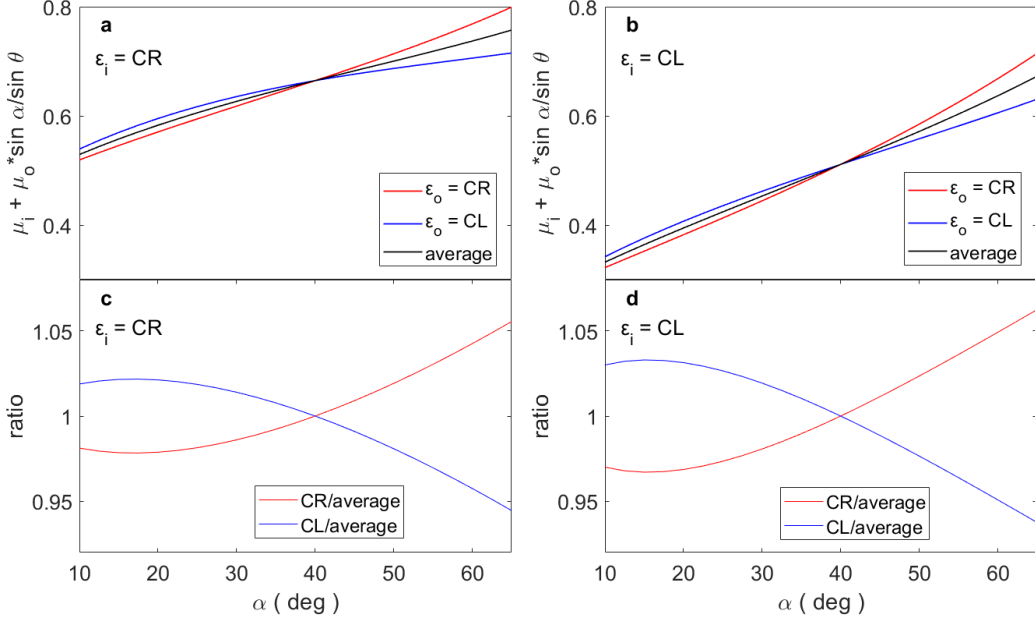


Figure S2. The angle dependence of the self-absorption factor (denominator in equation A3) at $E_o = 0.1$ eV. (a) The angle dependence for CR (red) and CL (blue) outgoing polarizations and their average (black) with CR incidence polarization. (b) The same as (a) but with CL incident polarization. (c) and (d) show the ratio between the self-absorption factor of CR (CL) outgoing polarization and the average self-absorption factor.

III. Polarization factors in RIXS cross-section for spin-wave excitations

As shown in the Methods of the main text, the RIXS cross-section for spin wave excitations is described by equation (4) with polarization factors $P_a^* P_b$. In the scattering geometry as in Fig. 1c of the main text, we define the polarization vectors for incident and outgoing X-Ray as:

$$\begin{aligned}
 \epsilon_{i,L} &= \frac{-i \sin \alpha, 1, -i \cos \alpha}{\sqrt{2}} \\
 \epsilon_{i,R} &= \frac{i \sin \alpha, 1, i \cos \alpha}{\sqrt{2}} \\
 \epsilon_{o,L} &= \frac{i \sin(\alpha + \beta), 1, i \cos(\alpha + \beta)}{\sqrt{2}} \\
 \epsilon_{o,R} &= \frac{-i \sin(\alpha + \beta), 1, -i \cos(\alpha + \beta)}{\sqrt{2}}
 \end{aligned} \tag{A4}$$

Here the L and R indicate the CL and CR polarizations, respectively. For ferromagnets with moments along x direction, we only consider the transverse excitations, i.e., S^{yy} , S^{zz} , S^{yz} and S^{zy} . The RIXS cross-sections for different incident and outgoing circular polarizations can be written as:

$$\begin{aligned}
I_{c_i, c_o} = & (\sin \beta)^2 \cdot S^{yy}(\mathbf{q}, \omega) + [c_o \cdot \sin \alpha - c_i \cdot \sin(\alpha + \beta)]^2 \cdot S^{zz}(\mathbf{q}, \omega) \\
& + [c_o \cdot \sin \alpha - c_i \cdot \sin(\alpha + \beta)] \cdot \sin \beta \cdot iS^{yz}(\mathbf{q}, \omega) \\
& - [c_o \cdot \sin \alpha - c_i \cdot \sin(\alpha + \beta)] \cdot \sin \beta \cdot iS^{zy}(\mathbf{q}, \omega)
\end{aligned} \tag{A5}$$

Here $c_{i(o)} = +1$ or -1 for CL or CR polarizations, respectively.

IV. Correcting low-energy RIXS MCD for spin-wave excitations by self-absorption and polarization factors

The diffuse reflections from the sample surfaces, which contribute to the elastic scattering at zero-energy loss, are neither affected by the self-absorption effect nor the different circular polarizations. To completely subtract their contributions and obtain the correct profiles of the low-energy spin excitations, we first do the direct subtraction between the measured RIXS spectra of CR and CL polarizations without doing any corrections in advance. The obtained differences (RIXS MCD) contain the pure signals from the sample but are still influenced from both self-absorption and polarization factors. As the absorption coefficients and polarization factors of spin-wave excitations are all known, we can then exactly correct the low-energy RIXS MCD and obtain the profiles for the spin-spin correlations $S(\mathbf{q}, \omega)$. Below we show how the corrections are done for the low-energy RIXS MCD. For ferromagnetic spin waves in our Fe_3Sn_2 sample, $S^{yy} = S^{zz} = iS^{yz} = -iS^{zy} \equiv S(\mathbf{q}, \omega)$. According to equation A5, we therefore have a total polarization factor defined by the scattering angles:

$$\begin{aligned}
p(\boldsymbol{\epsilon}_i, \boldsymbol{\epsilon}_o, \alpha, \beta) = & (\sin \beta)^2 + [c_o \cdot \sin \alpha - c_i \cdot \sin(\alpha + \beta)]^2 \\
& + 2[c_o \cdot \sin \alpha - c_i \cdot \sin(\alpha + \beta)] \cdot \sin \beta
\end{aligned} \tag{A6}$$

The self-absorption correction factor for distinct incident and outgoing polarizations is:

$$s_a(E_i, E_o, \boldsymbol{\epsilon}_i, \boldsymbol{\epsilon}_o, \alpha, \theta) = \frac{1}{\mu(E_i, \boldsymbol{\epsilon}_i, \mathbf{k}_i) + \mu(E_o, \boldsymbol{\epsilon}_o, \mathbf{k}_o) \cdot \sin \alpha / \sin \theta} \tag{A7}$$

With the two factors, we can get the relation between the direct RIXS MCD cross-sections and the spin-spin correlations of spin waves:

$$I_{\text{direct-MCD}} = \left[\sum_{\boldsymbol{\epsilon}_o} p(\boldsymbol{\epsilon}_i, \boldsymbol{\epsilon}_o) \cdot s_a(\boldsymbol{\epsilon}_i, \boldsymbol{\epsilon}_o) - p(\boldsymbol{\epsilon}'_i, \boldsymbol{\epsilon}_o) \cdot s_a(\boldsymbol{\epsilon}'_i, \boldsymbol{\epsilon}_o) \right] \cdot S(\mathbf{q}, \omega) \tag{A8}$$

V. Fitting of the spin-wave excitations

Fitting by two damped harmonic oscillators

We first fit the low-energy RIXS-MCD spectra by two damped harmonic oscillators with free amplitudes, frequencies, and damping factors. The fitting energy range is $[-0.32 \text{ } 0.32]$ eV to avoid the influences from the tails of the high-energy fluorescence. The damped harmonic oscillators are convolved with a resolution function of Voigt profile (FWHM = 74 meV, Gaussian standard deviation $\sigma=24.3$, Lorentzian HWHM $\gamma=13.7$; these parameters are determined by fitting the elastic peak measured on a carbon tape). Figure S3a-b show the corrected RIXS-MCD spectra together with fitting curves. Figure S3c shows the integrated intensities of the fitted peaks. Figure S3d shows the peak maximum positions of the two fitted

peaks, which are also overlaid on the simulated spin wave dispersion in Fig. 1b of the main text. Figure S3e shows the fitted damping factors.

Two-mode fitting with fixed dispersion according to the Heisenberg model

The peak dispersions obtained in the above fitting by two damped harmonic oscillators agree very well with the acoustic and flat modes in the simple Heisenberg model with only a nearest neighbour exchange interaction $J_1 \sim 25$ meV. It is therefore reasonable to treat the small deviations of the peak positions from the calculated dispersion as fluctuations and fix them according to the Heisenberg model in the fitting. In this way, we can better examine how the spin excitation damping factors evolve. We assume a zero-energy offset in the fitting model to account for the errors in determining the zero-energy-loss positions. The fitting is done for different values of J_1 , and its value is determined as 24.7 meV according to the minima of the sum squared error of the fitting for all spectra. The fitting results are displayed in figure S4 and figure 4 in the main text. Figure S4c shows the zero energy offsets of the fitting, which are very small ($\lesssim 4$ meV) and indicate that the fitting is in a reasonable range. The integrated intensities and the fitted damping factors are shown in Fig. 4b and 4c of the main text, respectively.

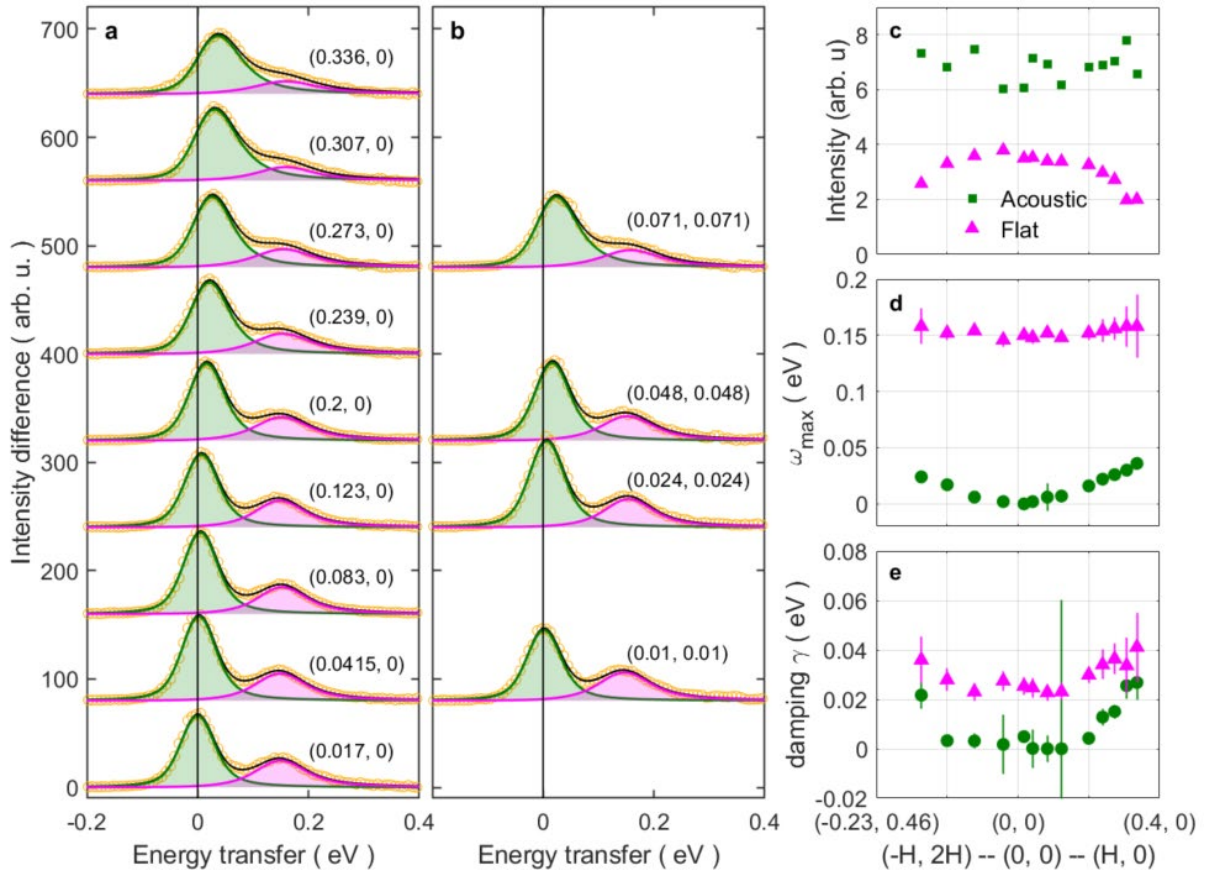


Figure S3. (a) and (b) The low-energy RIXS-MCD spectra (orange circles) and the fitting curves by two damped harmonic oscillators (green and magenta lines). (c) The integrated intensities (peak areas) of the fitted acoustic mode (green circles) and the flat mode (magenta triangles). (d) The fitted peak maximum positions of the two modes. (e) The fitted damping factors γ of the two modes.

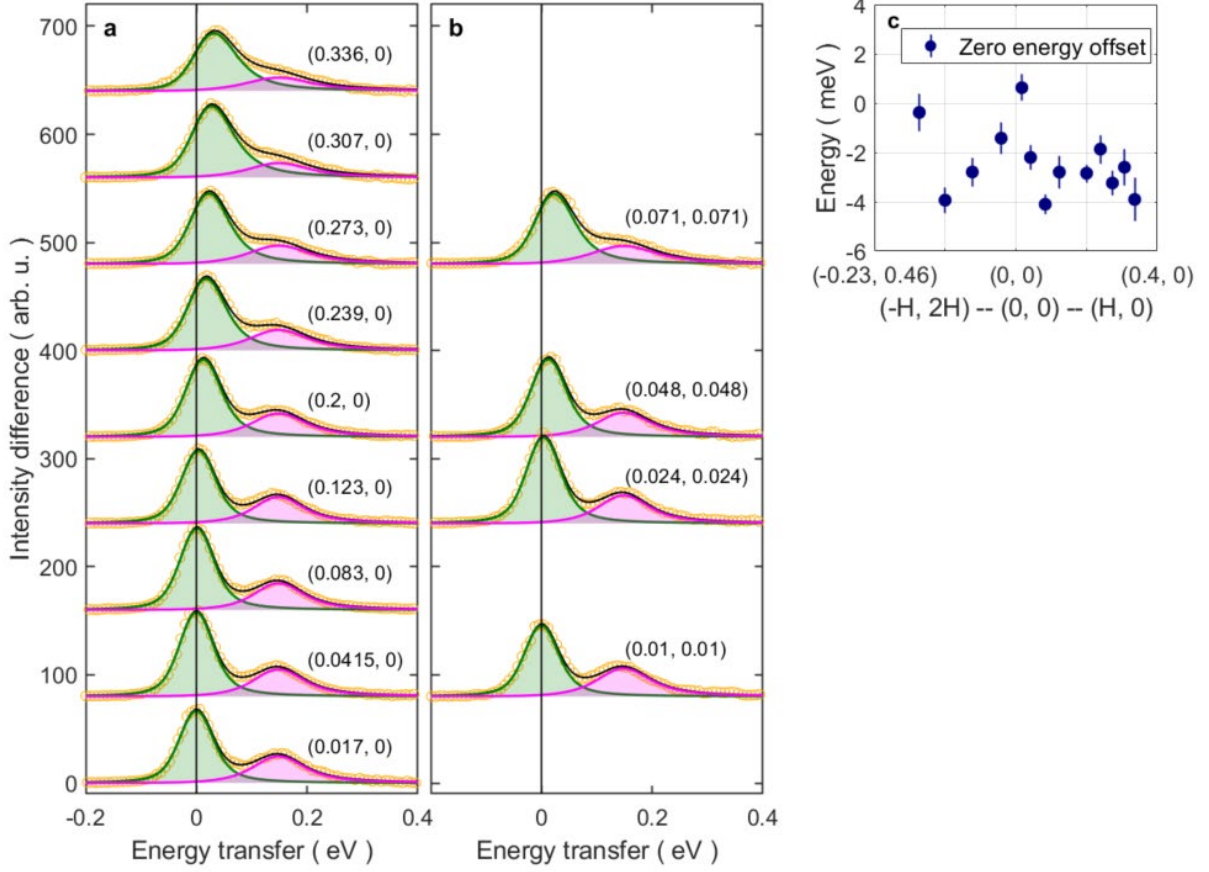


Figure S4. (a) and (b) The low-energy RIXS-MCD spectra (orange circles) and the fitting curves by two damped harmonic oscillators (green and magenta lines) with fixed peak positions according to the Heisenberg model with $J_1=24.7$ meV. (c) The zero energy offsets obtained in the two-mode fitting. The intensities and the damping factors of this fitting are presented in Fig. 4b and 4c of the main text.

Comparison of two-mode to three-mode fitting including dispersive optic mode

The Heisenberg model on the kagome ferromagnet actually displays three branches of spin waves, with an additional dispersive optic mode which converges to the flat mode in the long wavelength limit, as shown in figure 1b in main text. Here we try to add this third mode into the fitting for two spectra with the largest momenta and compare the results to those for the two-mode fitting. We still fixed the peak positions according to the Heisenberg model with $J_1=24.7$ meV. To further reduce the number of fitting parameters, we assume that the amplitudes and damping factors of the dispersive mode are equal to those of the flat mode. Because of the mode convergence as $q \rightarrow 0$, this three-mode description will be no different than the two-mode description except for the highest momenta probed, where a spectral weight filling, due to the downward dispersing optic mode, would be expected between the flat and acoustic modes. We therefore focus on $\mathbf{q} = (0.336, 0)$ and $(0.307, 0)$, for which the two- and three-mode fitting results are shown in figure S5. Involving the third mode makes the fits marginally worse in the sense that they present an oversmoothed optic mode signal superposed on the tail of the acoustic modes: the three-mode fit slightly overshoots the data between the acoustic and flat mode peaks, and then slightly undershoots on the high energy side of the flat mode. That the data do not require an appreciable contribution from the dispersive optic mode

is further demonstrated by figure S5c and f, where we remove the restriction on the amplitudes of the dispersive optic mode to let them float. The amplitudes of the dispersive optic mode tend to go to slightly negative values -0.26 ± 0.84 and -0.28 ± 0.75 for $q = (0.336, 0)$ and $(0.307, 0)$, respectively, in units where 1 is the amplitude of the flat optic mode, indistinguishable from zero.

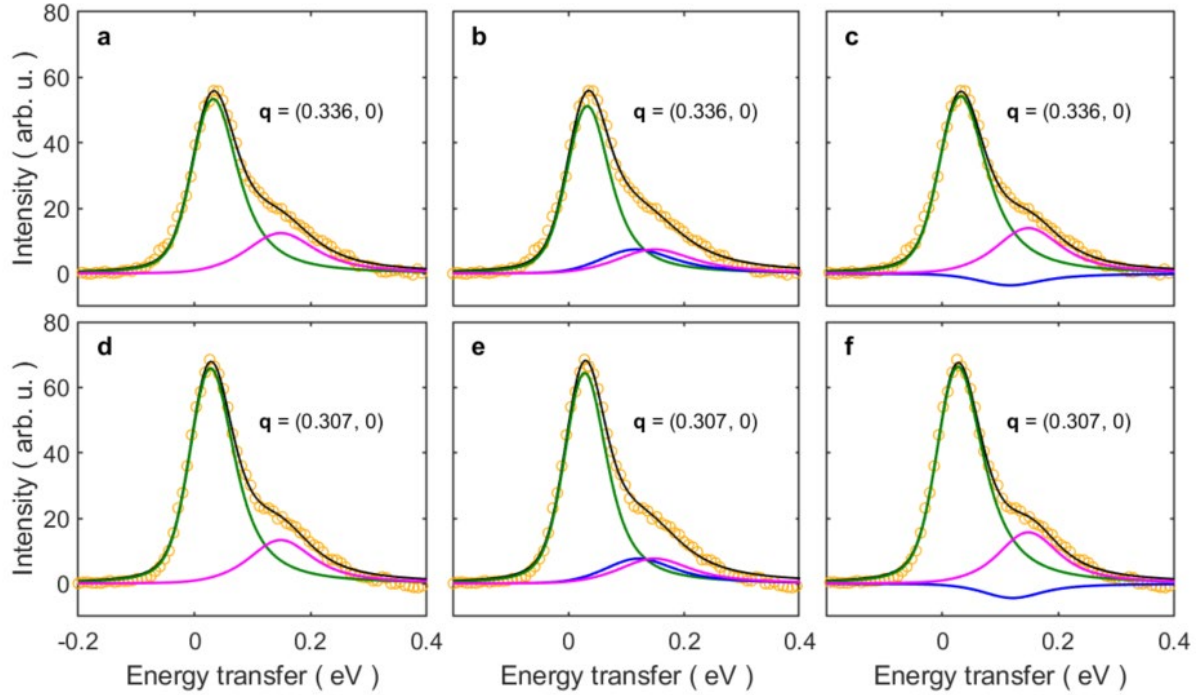


Figure S5 Comparison of the two-mode and three-mode fitting. (a) and (d) are the fitting results of the two-mode fitting. (b) and (e) are the three-mode fitting with the amplitudes and damping factors of the dispersive optic mode (blue lines) and flat mode (magenta lines) set to be equal. (c) and (f) represent also three-mode fitting, but the amplitudes of the dispersive optic mode and flat mode are varied independently.

References

1. Nakajima, R., Stöhr, J. & Idzerda, Y. U. Electron-yield saturation effects in L-edge X-ray magnetic circular dichroism spectra of Fe, Co, and Ni. *Phys. Rev. B* **59**, 6421–6429 (1999).
2. Henneken, H., Scholze, F. & Ulm, G. Lack of proportionality of total electron yield and soft x-ray absorption coefficient. *J. Appl. Phys.* **87**, 257–268 (2000).
3. Ruosi, A. *et al.* Electron sampling depth and saturation effects in perovskite films investigated by soft X-Ray absorption spectroscopy. *Phys. Rev. B* **90**, 125120 (2014).
4. Chabot-Couture, G. *et al.* Polarization dependence and symmetry analysis in indirect K-edge RIXS. *Phys. Rev. B* **82**, 035113 (2010).
5. Achkar, A. J. *et al.* Bulk sensitive X-Ray absorption spectroscopy free of self-absorption effects. *Phys. Rev. B* **83**, 81106(R) (2011).